Combined structural and photoluminescence study of SiGe islands on Si substrates: comparison with realistic energy level calculations

2009 New J. Phys. 11 063021

(http://iopscience.iop.org/1367-2630/11/6/063021)

New Journal of Physics
The open-access journal for physics

Combined structural and photoluminescence study of SiGe islands on Si substrates: comparison with realistic energy level calculations

M Brehm[1], T Suzuki[1], T Fromherz[1,3], Z Zhong[1,2], N Hrauda[1], F Hackl[1], J Stangl[1], F Schäffler[1] and G Bauer[1]

[1] Institute of Semiconductor and Solid State Physics, University Linz, A-4040 Linz, Austria
[2] Surface Physics Laboratory (National Key Laboratory) and Department of Physics, Fudan University, Shanghai 200433, People's Republic of China
E-mail: thomas.fromherz@jku.at

New Journal of Physics **11** (2009) 063021 (15pp)
Received 25 February 2009
Published 12 June 2009
Online at http://www.njp.org/
doi:10.1088/1367-2630/11/6/063021

Abstract. The Stranski–Krastanow growth of SiGe islands by deposition of SiGe alloys instead of pure Ge allows us to control both the Ge concentration and gradient in the islands. In contrast to the commonly found increasing Ge content with island height, growth conditions for islands with nearly constant and even decreasing Ge profile along the growth direction were found. Atomic force microscopy, transmission electron microscopy and high-resolution x-ray diffraction were employed to determine the islands' size, shape, lateral distance and Ge composition. Efficient photoluminescence is emitted from these islands. We show that for islands with higher Ge contents at the bottom than at the apex, transitions between heavy holes and electron Δ_{xy} states in the compressive Si regions *around* the island's *circumference* dominate the photoluminescence spectra instead of the usually observed recombination between heavy holes and electrons in the Δ_z valleys in the tensile Si *above* the island's *apex*. The relative importance of the Δ_{xy} transitions is enhanced for lateral island distances less than 10 nm, where overlapping strain fields of neighbouring islands increase the compressive strain in the Si region between them. At intense photoexcitation, recombinations between electrons in the Δ_z valleys and light holes within the islands appear in the photoluminescence spectra. These so far, for SiGe islands, unobserved transitions were identified by a quantitative modelling of the band

---

[3] Author to whom any correspondence should be addressed.

structure within the islands and in the surrounding Si matrix based on full 3D simulations using the nextnano^3 package with the experimentally obtained island shape and composition as input parameters.

Contents

1. Introduction

The necessity of adding optoelectronic building blocks to the standard Si CMOS technology for managing the ever growing amount of data is well documented in the literature [1, 2]. Although Si/Ge-based, monolithically integrated modulators [3] and detectors [4] with competitive bit rates up to 30 Gb s^{-1} have been realized, as efficient electrically driven radiation sources only *hybrid* solutions based on III–V lasers bonded to an SOI platform have been demonstrated up to now [5].

For the *monolithic* integration of emitters into Si-based electronics, SiGe quantum dots have been identified as promising candidates, since the three-dimensional (3D) confinement of electrons and holes enhances the probability of photon emission that is low in Si and Ge bulk crystals because of the indirect nature of their fundamental band gap. Thus, photoluminescence (PL) from self-assembled Ge islands (grown in the Stranski–Krastanow growth mode) on (001) Si substrates has been studied ever since their first observation (see for example [6]–[18]). As an important step towards applications, it has been shown that the statistical size distribution and thus the inhomogeneous broadening of the PL emission spectrum of an island ensemble can be reduced by pre-structuring of the Si substrates [19]–[22]. However, despite the large amount of data collected by many authors, a systematic comparison of the optical data with realistic band structure calculations for the islands and the surrounding Si substrate and Si capping layer is still lacking. In this paper, we aim to fill this gap with a systematic study of SiGe island growth, their structural characterization using atomic force microscopy (AFM), transmission electron microscopy (TEM) and x-ray diffraction (XRD) studies, PL investigations at low temperature and an explanation of the features observed in PL based on 3D band structure simulations for the islands and the surrounding Si matrix. In particular, by intentionally varying the Ge concentration in the islands along the growth direction, the localization of the hole ground state within the island was controlled. The influence of the localization of the holes on the overlap with the electron wave functions confined to the Si matrix (type II band alignment [11]), and thus on the PL efficiency, was investigated in three groups of samples containing islands with either increasing, almost constant or decreasing Ge concentration along the growth direction.

Table 1. Structural island parameters as determined from AFM and XRD experiments used as input parameters for the nextnano^3 [23] simulations. All SiGe alloy layers were grown at a temperature (rate) of 650 °C (0.2 Å s^{-1}).

Sample	Radius (nm)	Height (nm)	h_{const} (nm)	$x_{\mathrm{Ge,bot}}$ (%)	$x_{\mathrm{Ge,top}}$ (%)
A	65	33	4.6	28	55
B	90	30	3.6	40	38
C	81	31	5	39	36
D	90	39	0	36	20
E	103	49	15	31	20
F	90	37	9.6	34	16

The paper is organized as follows: in section 2, we present the results on the molecular beam epitaxial growth of the islands and their structural characterization emphasizing the small lateral distance of the islands in our samples. In section 3, the PL spectra and the large observed PL efficiency are discussed; in section 4, the results of the band structure calculations for the heavy hole (HH) and light hole (LH) states within the islands, for the Δ_z and Δ_{xy} conduction band states in the compressively and tensile strained Si around the islands and for the influence of the *lateral island distance* on these states are presented. In section 5, we compare the measured PL spectra with the calculated transition energies, emphasizing the influence of localization of HH and LH states within an island on the observability of the PL transitions; finally, we summarize our findings in section 6.

2. Growth and structural investigations

SiGe islands were grown by solid source molecular beam epitaxy (MBE) in the Stranski–Krastanow growth mode. On top of (001) Si substrates, first a Si buffer layer was deposited at temperatures ramping from 550 to 650 °C and at a growth rate of 1 Å s^{-1}, followed by deposition of SiGe alloys. During SiGe deposition the Ge content was either increased or decreased with different gradients. Together with the intermixing and Ge segregation during deposition, different Ge gradients in the islands result, as determined by XRD (see table 1). The growth rate and temperature of the SiGe alloy was kept constant at 0.2 Å s^{-1} and 650 °C, respectively. A constant Si and Ge flux reflecting the target alloy composition at the base of the island was initially kept until island nucleation was observed in the reflection high-energy electron diffraction (RHEED) pattern. The thickness of this layer with constant alloy composition $x_{\mathrm{Ge,bot}}$ is given for the various samples by h_{const} in table 1. Subsequently, the Ge flux was ramped to reach the Ge content $x_{\mathrm{Ge,top}}$ at the top of the islands given in table 1. After island growth was completed, a part of the wafer intended for AFM measurements was covered by a mechanical shutter before the capping with Si was initiated. After a growth interruption of ~5 min during which the substrate temperature was decreased to 450 °C, the growth of the Si capping layer was started. After 10 nm Si deposition the temperature was ramped up to 650 °C during growth. This procedure ensured that the dot shape, size and composition did not suffer a substantial change during capping, while at the same time the defect density was kept low. The total Si capping layer thickness for all samples was 150 nm.

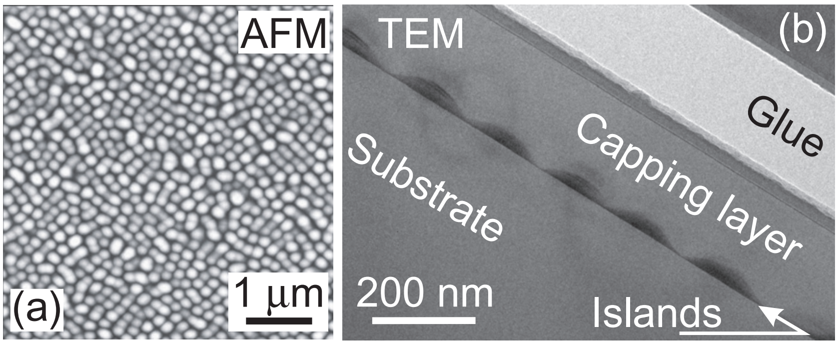

Figure 1. AFM (a) and TEM (b) images of sample B indicating small lateral inter-island distances and large, dislocation-free islands.

The surface morphology of the uncapped region of each sample was investigated by AFM in the tapping mode. A typical AFM picture obtained from sample B is shown in figure 1(a). The SiGe islands have a dome shape with dominant {1, 1, 3} and {15, 3, 23} facets. For the growth conditions employed, a relatively high density of the SiGe islands in the range $2\text{–}4 \times 10^9\,\text{cm}^{-2}$ is observed. As a consequence of the high density and the large base diameters of the domes in the range between 130 and 200 nm, in all samples the islands nearly touch each other. A similar surface morphology of domes formed during SiGe deposition is reported in [24]. Some of the samples were investigated by cross sectional TEM. As an example, in figure 1(b) the TEM micrograph for sample B is shown. From figure 1, it is evident that the 2D layer of thickness h_{const} that was grown with constant Ge composition is virtually completely integrated into the island most probably via trench formation around the islands [24]. Owing to the small inter-island distance, it cannot be conclusively judged on the basis of the TEM pictures whether or not a few-mono-layers-thick wetting layer (WL) remains between the islands. However, the volume possibly occupied by such a WL is vanishingly small compared to the island volume and thus no WL is included in the simulations discussed in the following. In none of the islands were dislocations found in the TEM micrographs. In addition, the TEM data were used to check the inter-island spacings and island aspect ratios, and good agreement between the TEM data and the AFM data was found.

The AFM scans give the island sizes and information on the size distribution as well as on their mutual distance. To obtain the Ge distribution and the strain state in the islands, we performed XRD measurements. Reciprocal space maps (RSMs) around asymmetrical Bragg peaks were recorded for all samples. For samples with large SiGe island volumes, the in-house Seifert XRD3003 high-resolution diffractometer equipped with a Göbel mirror to increase the primary beam intensity provided a sufficient signal-to-noise ratio to record the RSMs. For other samples we used synchrotron radiation at beamline BW2 of HASYLAB in Hamburg, Germany. In the former case, a wavelength of 1.54 Å (Cu K_α radiation) was used, and the intensity was recorded by a linear position-sensitive detector, giving a dynamic range of five orders of magnitude. In the latter case, a shorter wavelength of 1.24 Å was used to reduce atmospheric attenuation, and the scattered radiation was recorded using a 2D position-sensitive detector, giving a dynamic range of seven orders of magnitude. RSMs are shown in figure 2. Besides the Si substrate peak (labelled ‘Si’), diffuse scattering from the partially relaxed SiGe islands (labelled ‘SiGe’) is clearly visible.

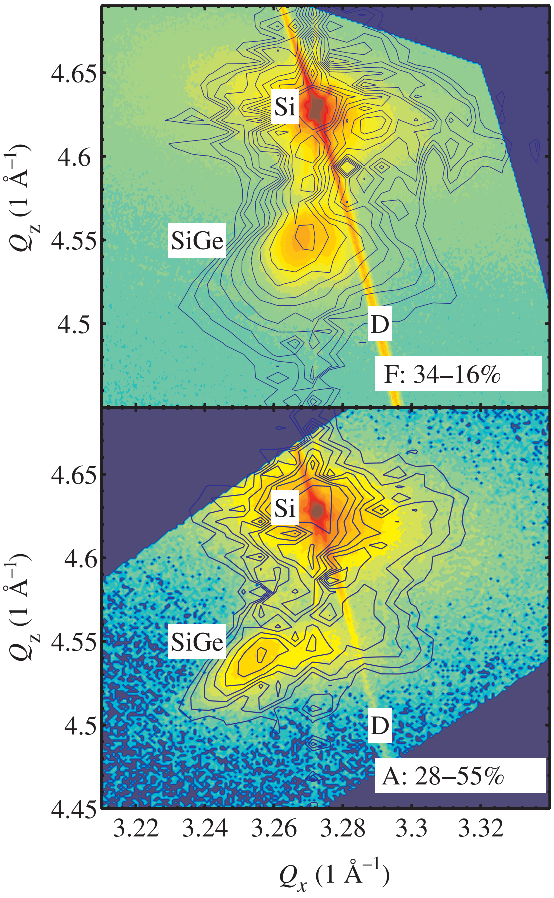

Figure 2. XRD RSMs around the (2, 2, 4) Bragg reflection for samples A and F. The labels Si and SiGe refer to the signal from the Si substrate and from the partially relaxed SiGe islands, respectively. The intense lines labelled D are detector array artifacts due to the huge intensity of the Si substrate peak. The logarithm of the measured x-ray intensity is colour coded with dark red (blue), indicating maximum (zero) intensity. The results of the simulations are shown by the blue contour lines. For the heights and base diameters given in table 1 for samples A and F, the best fits were achieved assuming the Ge gradients given in the plot.

To analyse the XRD data, finite element modelling (FEM) was performed using the COMSOL multiphysics FEM suite. For the geometry of the SiGe islands we used the shape of a rotational paraboloid with heights and diameters as determined by AFM measurements. Neglecting the particular faceted shape of the island and approximating it with a round shape has no significant influence on the analysis, since the elastic relaxation is mainly governed by the aspect ratio of the islands [25, 26] and the Ge distribution. The Ge profile entered the simulations as a fitting parameter. We assumed linear profiles between the bottom and top Ge content values $x_{\mathrm{Ge,bot}}$ and $x_{\mathrm{Ge,top}}$ and no lateral Ge gradients. From the FEM simulations, we obtain the strain field inside the SiGe islands as well as the surrounding Si matrix. As discussed in a previous paragraph, no clear evidence of a WL was found by TEM. Also, in the

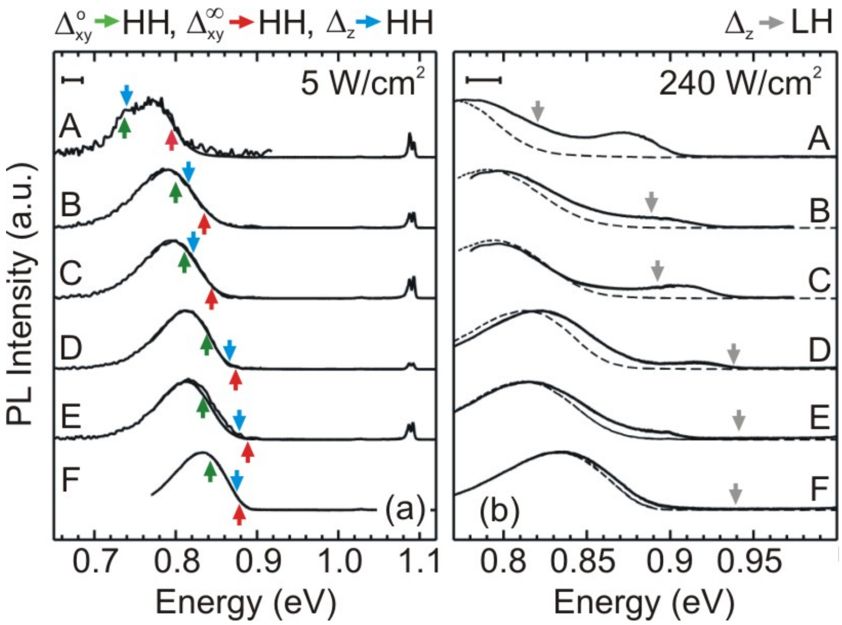

Figure 3. Low-temperature (10 K) PL spectra for samples A–F excited by an Ar^+ laser operating at 514 nm. Spectra measured at excitation intensities of 5 and 240 W cm^{-2} are shown by the full lines in (a) and (b), respectively. For comparison, in (b), also the spectra measured at 5 W cm^{-2} are shown by the broken lines. The arrows indicate calculated transition energies as described in the text. In (a), the green and red arrows mark transitions from Δ_{xy} to HH states. For the green arrow, the experimentally observed small lateral island distance (2 nm) and, thus, strongly overlapping strain fields were included (Δ_{xy}^{o}–HH transitions), whereas for the red arrows a large (100 nm) lateral island spacing and consequently non-overlapping strain fields were assumed (Δ_{xy}^{∞}–HH transitions). The blue arrows indicate the Δ_z–HH transitions. In (b), the grey arrows indicate the Δ_z–LH transitions. The error bars in the top left corners of both panels indicate the uncertainties in the calculated transition energies estimated from the uncertainties of the island parameters as discussed in the text.

PL spectra shown in figure 3 WL emission lines are absent. Thus the WL was also omitted in the FEM simulations. Using the strain distribution, we employed kinematical scattering theory to simulate the diffuse scattering pattern[4]. The Ge profile was then varied in a fitting loop to obtain the best correspondence between simulation and experiment (figure 2). This way the Ge and strain distribution are determined. In the FEM modelling, only *one* SiGe island is concerned, while in the XRD experiment a large *ensemble* of islands (typically $\sim 5 \times 10^5$) is illuminated. Since the islands are randomly distributed on the substrate, the scattered signal is the incoherent superposition of the scattering from each individual island, and hence is proportional to the scattered intensity from a single island. However, it turned out to be crucial in the simulations to take into account the close proximity of the islands, due to which their individual strain fields overlap. This was accomplished by restricting the FEM modelling

---

[4] For a review see [27].

to a region centred around the island and exceeding its diameter in the [1 0 0] and [0 1 0] directions by the average inter-island distance (i.e. by 2–4 nm). On this region's (1 0 0), ($\bar{1}$ 0 0), (0 1 0) and (0 $\bar{1}$ 0) boundaries, the normal component of the displacement field was required to vanish as those planes represent symmetry planes between adjacent islands. Only with these FEM boundary conditions modelling the small distance between the islands are the diffraction patterns reproduced with sufficient precision. Figure 2 shows as representative examples the XRD data of samples A and F together with the corresponding simulations based on the fitting parameters listed in table 1.

3. PL spectra

The PL spectra of samples A–F shown in figure 3 were measured for a sample temperature of 10 K using the 514 nm line of an Ar^+ ion laser at an intensity of 5 W cm^{-2} for the excitation. The spectra were recorded using an InGaAs line detector for energies above 0.78 eV. To access also the energy range below 0.78 eV, an InAs single element detector was used together with a lock-in amplifier. In the spectra of all samples, a clear SiGe island-related PL signal is observed in the spectral range between 0.7 and 0.9 eV together with the characteristic PL emission of the Si substrate close to 1.1 eV. A comparison of the intensities of the island-related signals and the Si substrate signals indicates that the PL emission of the islands is rather intense, keeping in mind that only one island layer is present in our samples. Depending on the sample composition, this intense island emission can be shifted over a large part of the spectral region important for telecommunication, and is reduced only by a factor of two by raising the sample temperature from 10 K up to 77 K (not shown in figure 3).

In the region between 0.78 and 1 eV, additional spectra under a higher excitation intensity of 240 W cm^{-2} were measured. These spectra are shown by the full lines in figure 3(b) together with the spectra measured under 5 W cm^{-2} excitation intensity (broken lines). From a comparison of the spectra it becomes evident that increasing the excitation intensity results in both a broadening of the island-related emission also present at low excitation intensities, and in the appearance of an additional emission band blue-shifted with respect to the low-excitation-intensity PL band. This additional band is most prominently observed for samples A, B and C, weakly present for D and absent for samples E and F. In the following sections, we compare these experimental findings with the results of energy level calculations for the SiGe islands and show how they can be correlated with the Ge profiles in the various samples (listed in table 1) that were intentionally established during growth.

4. Calculation of transition energies

The radiative transitions in this Si/Ge system are indirect both in real and reciprocal space. Thus, to fully understand the transitions observed in a PL experiment, the complexity of the confinement situation for electrons and holes in these structures has to be taken into account. This has been done based on the simulation package nextnano^3 [23]. Within nextnano^3, in a first step, the strain fields in the SiGe islands and the Si matrix are calculated by minimizing the elastic energy. In this calculation, the bulk lattice constant of SiGe alloys was calculated according to Vegard's law [28] and the elastic constants given in table 2 were used. The strain fields calculated by nextnano^3 are in excellent agreement with those calculated for the

Table 2. Material parameters used in the simulations. The values for a SiGe alloy are calculated by linear interpolation from the respective values for Si and Ge.

	Si	Ge
Deformation potentials (eV) [29]		
Δ-valley, hydrostatic (absolute, a_c)	3.3	2.55
Δ-valley, uniaxial (Ξ_u^Δ)	8.6	9.42
Valence band, hydrostatic (absolute, a_v)	1.8	1.24
Valence band, [100]-uniaxial (b)	−2.1	−2.86
Valence band, [111]-uniaxial (d)	−4.85	−5.28
Effective masses		
Δ-valley, transverse ($m_{\Delta,t}$) [30]	0.19	0.195
Δ-valley, longitudinal ($m_{\Delta,l}$) [30]	0.916	0.93
HH, spherically averaged (m_{HH}) [31]	0.54	0.34
LH, spherically averaged (m_{LH}) [31]	0.15	0.043
Elastic constants (GPa) [32]		
c_{11}	165.77	128.53
c_{12}	63.93	48.62
c_{44}	79.62	66.80

simulation of the XRD results (using the FEM simulation package). As an example, the non-vanishing components (ε_{xx}, ε_{yy}, ε_{zz}, ε_{yz}) of the strain tensor in the [010] × [001] symmetry plane of sample B are shown in a 3D plot in figure 4. Due to the elastic relaxation of the SiGe island, the strain in the Si matrix above and below the island is compressive along the growth direction, whereas along the circumference it is compressive in the lateral direction. Within the SiGe island, lateral compressive strain dominates. Figure 4 also shows the type of rectangular, manually set mesh that was used for the nextnano^3 simulations. Mesh spacings between 2.75 and 11 nm (0.5 and 10 nm) were used in the lateral (growth) direction, the denser mesh regions being located in and in the vicinity of the island, where wave functions are expected to be localized.

In a second step of the nextnano^3 simulations, the strain-induced spatial variation and splitting of the conduction and valence band edges are calculated by linear deformation potential theory. The deformation potential constants for SiGe were obtained by linear interpolation between the respective values for Si and Ge given in table 2. The band offset between the average of the Si and $\mathrm{Si}_{1-x}\mathrm{Ge}_x$ valence bands for unstrained bulk crystals [$E_{\mathrm{av}} = E_{\mathrm{av}}(\mathrm{SiGe}) - E_{\mathrm{av}}(\mathrm{Si})$] was calculated according to $E_{\mathrm{av}} = 580x$ (meV) [29]. The unstrained band gap of a SiGe alloy was calculated according to [33]. Using these equations, the total variation of the conduction and valence band edges as a function of the 3D position in and around the island is calculated as outlined in [29]. Due to strain, the six-fold degeneracy of the Si Δ conduction band minima is locally lifted into three two-fold degenerated valleys (Δ_x, Δ_y, Δ_z) oriented along the [100], [010] and [001] reciprocal space directions. In addition, also the degeneracy of the HH and LH valence band edges is lifted.

In the last step of the nextnano^3 simulations, in each of these 3D potential landscapes, a single band, effective mass Schrödinger equation is solved for the Δ_x, Δ_y, Δ_z, HH and LH wave

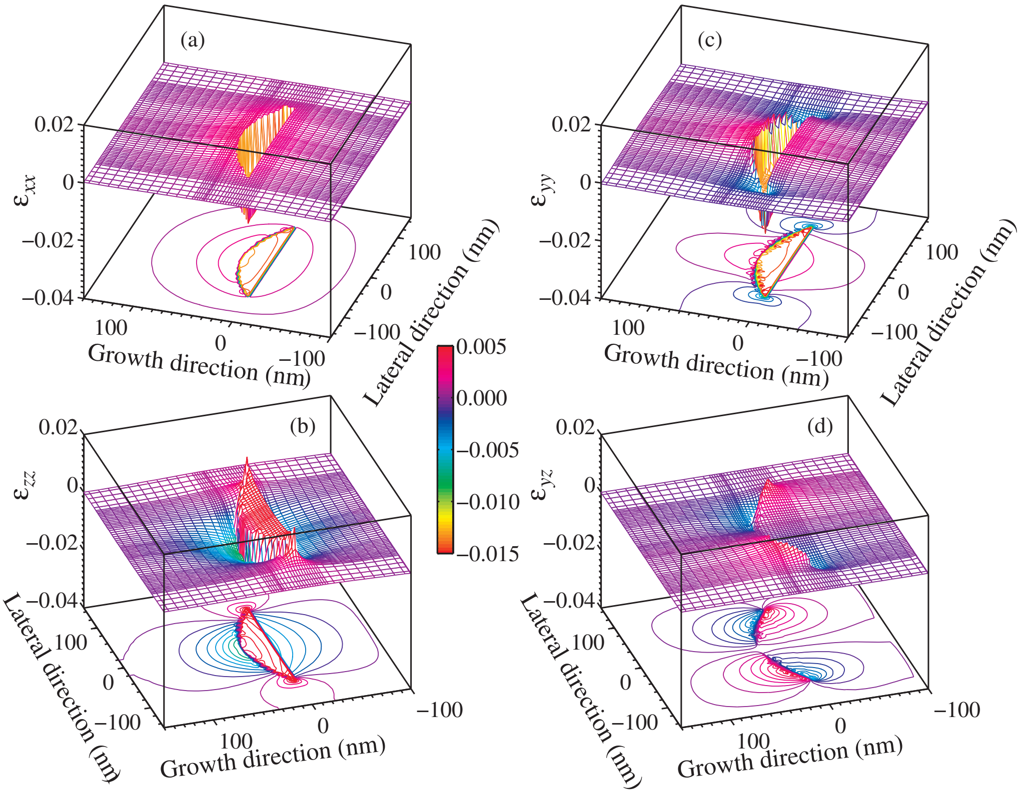

Figure 4. Non-vanishing components of the strain tensor (ε_{xx}, ε_{yy}, ε_{zz} and ε_{yz}) in the [010] × [001] symmetry plane of sample B. For all samples, meshes similar to that shown in the 3D surfaces were used for the nextnano^3 simulations.

functions and eigenenergies using the effective masses listed in table 2. In figure 5, the results of these calculations based on the structural parameters listed in table 1 are shown as 3D iso-surface plots for samples A–F on common x, y, z scales. The parabolic surface of the islands is shown in yellow. Non-yellow surfaces confine spatial regions within which the squared moduli of the wave functions ($\psi^*\psi$) are larger than $0.03\,\max(\psi^*\psi)$. The blue, red and grey surfaces refer to the Δ_z, HH and LH wave functions, respectively. The green surfaces confine the Δ_{xy} wave functions. A comparison of figures 4 and 5 shows that the Δ_z ground state is located in the Si regions above the apex of the island where the Si is compressively strained along the growth direction, whereas the Δ_{xy} ground states are localized in the Si matrix around the base circumference of the islands in the regions of large lateral compressive strain. Both HH and LH ground states are confined to the interior of the islands. Their relative distributions within the island are determined by an interplay between Ge profile and strain as will be discussed in more detail in section 5.

Note that in the results of the nextnano^3 calculations shown in figure 5, the Δ-valleys in the two lateral directions are no longer degenerate nor do they show the HH states four-fold symmetry. This breaking of the symmetry is caused by the choice of periodic boundary conditions with different periods in $[1, 0, 0]$ and $[0, 1, 0]$ directions. In $[1, 0, 0]$ direction, a period only 2 nm larger than the island diameter is assumed. This choice of the period is consistent with the results of the AFM scans that show that the islands are nearly touching each other. Also, in

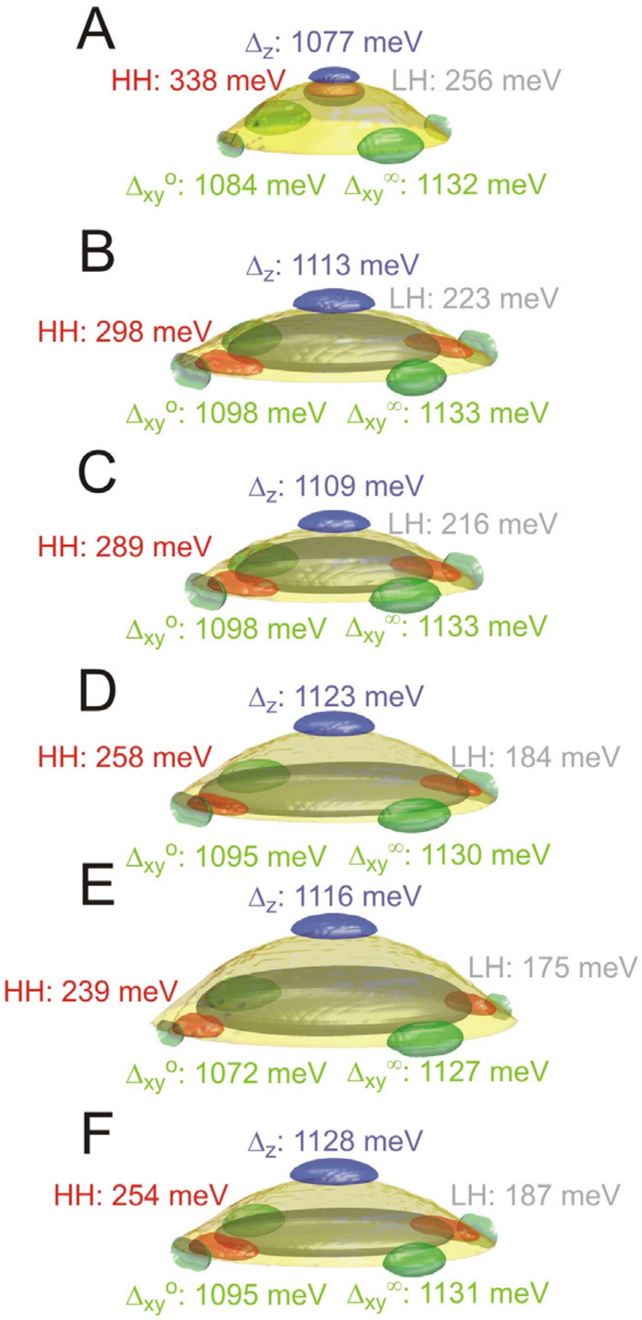

Figure 5. Iso-surface plot of the wave functions' squared moduli $\psi^*\psi$ and island surfaces (yellow) for samples A–F. The green, blue, red and grey surfaces confine regions in that $\psi^*\psi > 0.03\,\max(\psi^*\psi)$ for the Δ_{xy}, Δ_z, HH and LH states, respectively. The labels indicate the eigenenergies with respect to the average of the three valence bands at the Γ-point of an unstrained Si bulk crystal. In the lateral direction, periodic boundary conditions with 2 nm (100 nm) in $[1, 0, 0]$ ($[0, 1, 0]$) directions were assumed in order to investigate the influence of strongly (non) overlapping strain fields on the Δ^{o}_{xy} (Δ^{∞}_{xy}) eigenstate energies. This breaking of the four-fold lateral symmetry is also reflected in the plots of the HH wave functions.

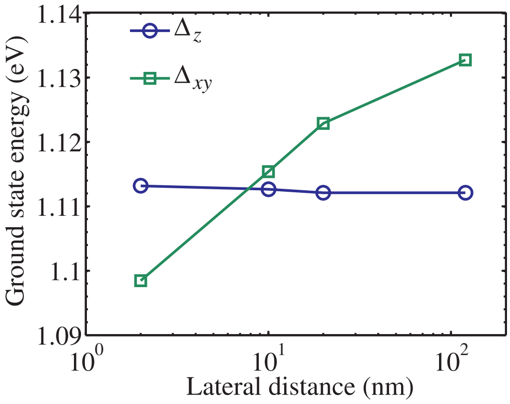

Figure 6. Variation of Δ_{xy} and Δ_z eigenenergy with lateral island distance for sample B. For distances smaller than 10 nm, the Δ_{xy} states become the electron ground states.

the simulations of the XRD, a 2–4 nm lateral separation of the islands had to be assumed as a prerequisite to achieve good agreement between measured and simulated XRD maps. In [0, 1, 0] direction, a 100 nm spacing between neighbouring islands was assumed in the calculations in order to quantify within one run of the computationally expensive simulation the influence of the strongly overlapping strain fields of the closely spaced islands on the energy levels of the Δ_{xy} valleys. As an example, the dependence of the Δ_{xy} and Δ_z ground state energies on the lateral period is shown in figure 6 for sample B. At a lateral island distance around 10 nm, the energy of the Δ_{xy} states is reduced below that of the Δ_z states so that below this distance the Δ_{xy} states become the electron ground states. In figure 5, the Δ_{xy} ground state energy calculated for strongly overlapping strain fields are labelled Δ_{xy}^{o}, whereas the results for isolated islands are given by the Δ_{xy}^{∞} values. The influence of the overlapping strain fields on the HH ground state energies is less significant. For samples A–F, typically only ~8 meV lower HH ground state energies are calculated if 100 nm island spacing is assumed instead of 2 nm. All labels in figure 5 refer to the ground state energies of the respective valleys, where the origin of the energy scale is set to the average energy of the three valence bands of unstrained bulk Si.

5. Analysis of the PL spectra

The identification of the observed PL transitions is based on the simulations of the ground state wave functions for electrons and holes shown in figure 5. The samples investigated in this work contain islands that can be grouped into three categories: islands with a significantly larger Ge content at the apex than at the base (positive Ge gradient, sample A), islands with almost constant Ge concentrations (samples B and C) and islands with a significantly smaller Ge concentration at the apex than at the base (negative gradient, samples D–F).

The sign of the Ge gradient most obviously determines the localization of the HH and LH ground states in the islands. For islands with a strong positive Ge gradient, both LH and HH wave functions are localized at the apex of the islands (A). For islands with nearly constant Ge concentration (B and C), the HH ground states are localized at the base circumference of the islands, whereas the LH states are repelled from the circumference due to the strain, but are otherwise smeared out over most of the island volume. In islands with negative Ge gradients (D–F), the LH states are in addition repelled from the apex of the island. Thus, they form a disc close to the islands' bases that remains radially separated from the HH states due to strain.

The overlap between the wave functions of the initial electron and the final hole states determines the luminescence efficiency between these states. Based on this rule, different transitions are expected to be dominant in islands with large positive and negative Ge gradient. As shown in figure 5, for islands with significantly positive Ge gradient (sample A), the largest overlap exists between Δ_z and HH ground states, whereas the overlap between Δ_{xy} and HH ground states is negligible. Thus we conclude that the PL emission of sample A at small excitation intensity (shown in figure 3(a)) is due to a Δ_z–HH transition. The corresponding PL transition energy is calculated by subtracting HH from Δ_z energy as given in figure 5. The result is indicated by the blue arrow in the PL spectrum labelled A in figure 3(a). Also shown in figure 3(a) are the calculated energy differences between the HH ground state and the states labelled Δ_{xy}^{o} and Δ_{xy}^{∞} in figure 5 by the green and red arrows, respectively. For sample A, the values of all three calculated transition energies are within the width of the observed PL band so that in this case experimentally no conclusions on the nature of the transition can be drawn.

As shown in figure 5, for nearly constant Ge concentration and negative Ge gradient the overlap of the HH ground state with the Δ_z states vanishes. Instead, a finite overlap between HH and the Δ_{xy} states is calculated. Thus, contrary to sample A we expect that Δ_z–HH transitions do not occur in these samples. Whether or not Δ_{xy}–HH transitions are observable instead depends then on the occupation of the Δ_{xy} states. For isolated islands with vanishing overlap of the strain fields of adjacent islands, the Δ_{xy} states would not be the electron ground states (compare Δ_{xy}^{∞} and Δ_z values in figure 5 for samples B–F) and, in this case, any Δ_{xy}^{∞}–Δ_z electron relaxation would effectively reduce the Δ_{xy}^{∞}–HH PL yield. However, the strain field overlap due to the dense packing of the islands in our samples results in a reduction of the Δ_{xy} ground state energies of samples B–F (zero and negative Ge gradient) below that of the Δ_z states (compare Δ_{xy}^{o} and Δ_z values in figure 5 for samples B–F). Thus, Δ_{xy}^{o}–Δ_z relaxations cannot occur and in this case an efficient Δ_{xy}^{o}–HH PL emission, as observed in samples B–F, is expected. Also the observed PL peak positions especially for the samples with negative Ge gradient (D–F) indicate Δ_{xy}^{o}–HH transitions, since the calculated energies of the Δ_z–HH and Δ_{xy}^{∞}–HH transitions (marked by the blue and red arrows in figure 3(a)) are significantly too large and only the calculated Δ_{xy}^{o}–HH energies (green arrows in figure 3(a)) fit reasonably. We want to point out that without the correct inclusion of the overlapping strain fields, for the samples with negative gradient (D–F) no convincing agreement between simulated and observed PL spectra could be achieved based on the measured structural parameters of the islands. The remaining small, seemingly systematic overestimation of the transition energies by the nextnano^3 calculations is most probably due to the uncertainties in the values for the absolute deformation potential parameters a_c and a_v listed in table 2. These parameters are the proportionality factors between the hydrostatic strain and the *absolute* energetic positions of conduction and valence bands in Si and Ge and thus are hardly accessible experimentally. Therefore, the values reported in the literature scatter considerably [29], [34]–[36]. In addition, exciton binding energies were not included in the calculation of the PL transition energies. In [37], a variational method for calculating the exciton binding energies for spherical type II QDs is presented. Following this work, the exciton binding energies for the present SiGe islands can be estimated to be smaller than 10 meV. Although the inclusion of the exciton binding energy would shift, for almost all samples (B–F), the calculated transition energy towards the observed transition energy, the size of this correction is regarded as insignificant compared to uncertainties in both the deformation potentials listed in table 2 and the structural parameters listed in table 1. Out of these structural parameters, the uncertainties in the Ge concentrations determine the uncertainties in the calculated transition energies most significantly, whereas the uncertainties in the island dimensions have a vanishing influence due to the small confinement energies of these large islands. Because of the localization of the holes in the Ge-rich region, the energies of those states are most sensitive to variations in the Ge concentration ($\sim 7\,\mathrm{meV}$ energy shift per percentage absolute concentration variation). From the analysis of the XRD maps as described in section 2, the Ge concentrations $x_{\mathrm{Ge,bot,top}}$ can be determined with an uncertainty of $\pm 1.5\%$ absolute, resulting in an uncertainty of the calculated PL transition energies of $\sim 20\,\mathrm{meV}$. Additionally, for the Δ^{o}_{xy}–HH energies, statistical variations of the inter-island distances cause uncertainty. From figure 6, this uncertainty is estimated at 15 meV, which corresponds to the variation of the inter-island distance between 2 and 8 nm, the latter distance being defined by the transfer of the ground state from the Δ^{o}_{xy} to the Δ_z valley. Thus, 25 meV results as an overall uncertainty for the Δ^{o}_{xy}–HH transition energy (indicated by the error bar in the upper left corner of figure 3(a)).

Figure 3(b) shows that at higher excitation intensity ($240\,\mathrm{W\,m^{-2}}$) a second PL peak at larger energies is observed for the samples with positive and with vanishing Ge gradient. From the energetic position, we ascribe this peak to an electron–LH transition. As shown in figure 5, the LH ground state has vanishing overlap with the Δ_{xy} states for all signs of the Ge gradient: for the islands with negative and vanishing Ge gradients (B–F), the LH states are repelled from the base circumference along which the Δ_{xy} (and HH) states are localized due to the strain. For positive Ge gradients, both HH and LH are localized at the apex of the islands, well separated from the Δ_{xy} states. Thus, no Δ_{xy}–LH recombination can be expected. On the other hand, for positive and vanishing Ge gradient, a finite overlap between Δ_z and LH states exists that becomes smaller as the Ge gradient becomes smaller. In the experimental data shown in figure 3(b), the calculated Δ_z–LH transition energies are marked by the grey arrows ($\sim 20\,\mathrm{meV}$ uncertainty in the arrow positions due to the uncertainty in the Ge concentration is indicated by the error bar in the top left corner of figure 3(b)). Except for sample A, the position of the additional peak agrees very well with the calculated Δ_z–LH transition energy. Moreover, the observed intensity of the PL signal at the calculated Δ_z–LH transition vanishes for the samples with negative gradient as predicted by our simulations. The good agreement of the calculated transition energies as well as the absence of the additional PL line for the samples with negative gradient confirm our assignment of this line to Δ_z–LH transitions.

6. Summary

A series of MBE-grown SiGe islands with intentionally varied Ge flux to realize different Ge gradients along the growth direction was investigated with respect to their structural and optical properties. Based on the simulation of XRD data, the Ge concentration gradients within the islands were determined consistently for all investigated samples. By a comparison with the results of nextnano^3 band structure calculations, the different Ge gradients allowed for an investigation of the influence of the regions of confinement for the electrons and holes on PL spectra, both as far as the recombination energies and the PL efficiency are concerned. In addition to the Δ_z–HH transitions involving electron states confined in the tensile strained Si close to the top of the island and heavy hole states confined within the islands, again close to their tops, for appropriate gradients Δ_{xy}–HH transitions were also observed. In this latter case the overlap is between electrons confined at the outer circumference of the islands, i.e. in the compressively strained Si regions with HH states, which are pushed downwards from the top to the circumference along the base of the islands. We showed that for the observation of these transitions a small lateral inter-island distance is decisive, which leads to an increased compressive strain in the Si regions in between the islands. For lateral inter-island distances below $\approx 10\,\mathrm{nm}$, these strain fields lower the energies of the Δ_{xy} states below those of the Δ_z states, resulting in Δ_{xy} electron ground states. The observation of additional PL features at higher energies for higher excitation intensity was attributed to the recombination of electrons in the Δ_z states with LH states situated in the centre of the islands.

Acknowledgments

This work was supported by the FWF within the SFB 'IROn' (projects F2502-N08, F2507-N08 and F2512-N08) and by the GMe, both in Vienna, Austria. Synchrotron XRD experiments were performed at BW2 and D4 beamlines of HASYLAB, DESY, Hamburg, Germany. We thank S Birner (nextnano^3, Munich, Germany) for support with the band structure calculations.

References

[1] Bautista J *et al* 2005 Silicon microphotonics *Microphotonics: Hardware for the Information Age* (http://mph-roadmap.mit.edu/index.php?option=com_content&view=article&id=61&Itemid=76: The Microphotonics Center at MIT) pp 1–30

[2] Fulbert L *et al* 2008 *A European Roadmap for Photonics and Nanotechnologies* (http://www.ist-mona.org/home.asp)

[3] Liu A, Liao L, Rubin D, Nguyen H, Ciftcioglu B, Chetrit Y, Izhaky N and Paniccia M 2007 *Opt. Express* **15** 660–8

[4] Morse M, Dosunmu O, Yin T, Kang Y, Sarid G, Ginsburg E, Cohen R and Zadka M 2008 *Proc. SPIE* **6996** 699614

[5] Fang A W, Park H, Kuo Y, Jones R, Cohen O, Liang D, Raday O, Sysak M N, Paniccia M J and Bowers J E 2007 *Mater. Today* **10** 28–35

[6] Apetz R, Vescan L, Hartmann A, Dieker C and Lüth H 1995 *Appl. Phys. Lett.* **66** 445

[7] Sunamura H, Shiraki Y and Fukatsu S 1995 *Appl. Phys. Lett.* **66** 953

[8] Schittenhelm P, Gail M, Brunner J, Nützel J F and Abstreiter G 1995 *Appl. Phys. Lett.* **67** 1292

[9] Schmidt O G, Lange C and Eberl K 1999 *Appl. Phys. Lett.* **75** 1905

[10] Schmidt O G, Lange C and Eberl K 1999 *Phys. Status Solidi* b **215** 319

[11] Schmidt O G and Eberl K 2000 *Phys. Rev.* B **62** 16715

[12] Wan J, Luo Y H, Jiang Z M, Jin G, Liu J L, Wang K L, Liao X Z and Zou J 2001 *Appl. Phys. Lett.* **79** 1980

[13] Brunner K 2002 *Rep. Prog. Phys.* **65** 27–72

[14] Vescan L and Stoica T 2002 *J. Appl. Phys.* **91** 10119

[15] Stoffel M, Denker U, Kar G S, Sigg H and Schmidt O G 2003 *Appl. Phys. Lett.* **83** 2910

[16] Xia J S, Ikegami Y, Shiraki Y, Usami N and Nakata Y 2006 *Appl. Phys. Lett.* **89** 201102

[17] Xia J S, Nemoto K, Ikegami Y, Shiraki Y and Usami N 2007 *Appl. Phys. Lett.* **91** 011104

[18] Baribeau J M, Rowell N L and Lockwood D J 2006 Self-assembled SiGe dots and islands *Self-Organized Nanoscale Materials* (New York: Springer) pp 1–52

[19] Zhong Z, Halilovic A, Fromherz T, Schäffler F and Bauer G 2003 *Appl. Phys. Lett.* **82** 4779

[20] Zhong Z and Bauer G 2004 *Appl. Phys. Lett.* **84** 1922

[21] Grützmacher D *et al* 2007 *Nano Lett.* **7** 3150–6

[22] Dais C, Mussler G, Sigg H, Fromherz T, Auzelyte V, Solak H H and Grüutzmacher D 2008 *Europhys. Lett.* **84** 67017
[23] Majewski J A, Birner S, Trellakis A, Sabathil M and Vogl P 2004 *Phys. Status Solidi* c **1** 2003
[24] Floro J A, Chason E, Freund L B, Twesten R D, Hwang R Q and Lucadamo G A 1999 *Phys. Rev.* B **59** 1990
[25] Hesse A, Stangl J, Holý V, Roch T, Bauer G, Schmidt O G and Denker U 2002 *Phys. Rev.* B **66** 085321
[26] Stangl J, Hesse A, Holý V, Zhong Z, Bauer G, Denker U and Schmidt O G 2003 *Appl. Phys. Lett.* **82** 2251
[27] Stangl J, Holý V and Bauer G 2004 *Rev. Mod. Phys.* **76** 725
[28] Salvador D D *et al* 2000 *Phys. Rev.* B **61** 13005
[29] de Walle C G V 2000 *Properties of Silicon Germanium and SiGe:Carbon (EMIS Data Review Series* vol 24) (London: INSPEC)
[30] Richard S, Aniel F and Fishman G 2004 *Phys. Rev.* B **70** 235204
[31] Yu P Y and Cardona M 1996 *Fundamentals of Semiconductors: Physics and Materials Properties* (New York: Springer)
[32] Madelung O, Rössler U and Schulz M (ed) 2001 *Group IV Elements, IV–IV and III–V Compounds (Landolt–Börnstein—Group III Condensed Matter* vol 41A1a) (Berlin: Springer)
[33] Braunstein R 1958 *Phys. Rev.* **109** 695
[34] Wei S H and Zunger A 1999 *Phys. Rev.* B **60** 5404
[35] Li Y H, Gong X G and Wei S H 2006 *Appl. Phys. Lett.* **88** 042104
[36] Li Y H, Gong X G and Wei S H 2006 *Phys. Rev.* B **73** 245206
[37] Laheld U E H, Pedersen F B and Hemmer P C 1995 *Phys. Rev.* B **52** 2697–703